



HAL
open science

Tapered vector Doppler for improved quantification of low velocity blood flow

Ingvild Kinn Ekroll, Vincent Perrot, Herve Liebgott, Jørgen Avdal

► **To cite this version:**

Ingvild Kinn Ekroll, Vincent Perrot, Herve Liebgott, Jørgen Avdal. Tapered vector Doppler for improved quantification of low velocity blood flow. *IEEE Transactions on Ultrasonics, Ferroelectrics and Frequency Control*, 2020, 10.1109/TUFFC.2020.3028874 . hal-03024630

HAL Id: hal-03024630

<https://hal.science/hal-03024630>

Submitted on 25 Nov 2020

HAL is a multi-disciplinary open access archive for the deposit and dissemination of scientific research documents, whether they are published or not. The documents may come from teaching and research institutions in France or abroad, or from public or private research centers.

L'archive ouverte pluridisciplinaire **HAL**, est destinée au dépôt et à la diffusion de documents scientifiques de niveau recherche, publiés ou non, émanant des établissements d'enseignement et de recherche français ou étrangers, des laboratoires publics ou privés.

Tapered vector Doppler for improved quantification of low velocity blood flow

Ingvild Kinn Ekroll, Vincent Perrot, Hervé Liebgott, Jørgen Avdal

Abstract—A new vector velocity estimation scheme is developed, termed Tapered Vector Doppler (TVD), aiming to improve the accuracy of low velocity flow estimation. This is done by assessing the effects of Singular Value Decomposition (SVD) and Finite Impulse Response (FIR) filters and designing an estimator which accounts for signal loss due to filtering. Synthetic data created using a combination of *in vivo* recordings and flow simulations were used to investigate scenarios with low blood flow, in combination with true clutter motion. Using this approach, the accuracy and precision of TVD was investigated for a range of clutter-to-blood and signal-to-noise ratios. The results indicated that for the investigated carotid application and setup, the SVD filter performed as a frequency based filter. For both SVD and FIR filters, suppression of the clutter signal resulted in large bias and variance in the estimated blood velocity magnitude and direction close to the vessel walls. Application of the proposed tapering technique yielded significant improvement in the accuracy and precision of near-wall vector velocity measurements, compared to non-tapered vector Doppler and weighted least squares approaches. In synthetic data, for a blood SNR of 5 dB, and in a near-wall region where the average blood velocity was 9 cm/s, the use of tapering reduced the average velocity magnitude bias from 26.3 cm/s to 1.4 cm/s. Complex flow in a carotid bifurcation was used to demonstrate the *in vivo* performance of TVD, and it was shown that tapering enables vector velocity estimation less affected by clutter and clutter filtering than what could be obtained by adaptive filter design only.

Index Terms—Adaptive clutter filtering, vector velocity estimation, tapered vector Doppler, blood flow imaging, low velocity blood flow, vector Doppler, quantitative vascular blood flow estimation, weighted least squares.

I. INTRODUCTION

Vector velocity imaging (VVI) of blood flow has been a topic of interest for ultrasound research since the 1970s. By combining VVI estimators with the use of broad beam acquisitions, it has become possible to produce vector velocity estimates in larger regions of interest with high frame rates. In recent years, the use of vector velocity imaging based on vector Doppler, transverse oscillations, speckle tracking or vector flow mapping has been investigated in applications ranging from assessment of tissue elasticity [1], [2], visualization of complex flow fields in the hearts of newborns, children and adults [3]–[6] as well as in the carotid arteries [7]–[9] and ascending aorta [10], mapping of vorticity and energy loss in

the left ventricle [11], [12] and mapping of flow complexity in the carotid bulb [13]. The widespread research utilizing 2D and 3D velocity estimation techniques indicates that the different approaches have matured in recent years and have the potential to provide additional diagnostic information in cardiovascular applications.

Though visualization of flow patterns already provides more information than the conventional color Doppler images, many applications would benefit from more quantitative measurements of blood velocities. Examples include grading of carotid stenoses [14], [15], volume flow measurements [16], and assessment of wall shear rate [17]. Whereas quantitative blood flow measurements are currently performed using spectral Doppler, vector velocity imaging techniques have the potential to improve diagnostic accuracy by providing measurements that are less dependent on the operator and ideally also independent of the flow angle. The use of vector velocity imaging for quantitative measurements is, however, still limited, because the underlying mean velocity estimates are associated with large bias and variance.

Due to reverberations and limitations in the spatial resolution of the system, signals from regions inside blood vessels will also contain interfering signal components from stationary and slowly moving tissue surrounding the vessels. Such signal components are typically suppressed using clutter filters before velocity estimation. However, designing clutter filters to improve velocity estimation accuracy is challenging. If the signal from tissue is not sufficiently attenuated before mean velocity estimation, it will lead to a bias towards zero velocity. Although residual clutter will reduce the variance of the resulting vector velocity field, the bias is highly unpredictable, hampering the usefulness of vector velocity imaging techniques for quantitative measurements. On the other hand, more aggressive clutter filtering often leads to removal of low velocity blood components from the signal, which in turn leads to increased variance and overestimation of both mean and vector velocities.

In addition, both blood velocities and tissue movement varies throughout the cardiac cycle, meaning that the optimal filter parameters may differ among frames. One way to address this problem is to adapt the clutter filter to the tissue motion. For filters with a well defined frequency response, this would mean varying the stopband and passband cutoff frequencies based on the velocities of the surrounding tissue, as was the suggested solution in e.g. [18]. However, in regions where blood and tissue velocities overlap, these filters can no longer provide accurate blood velocity estimates. Another approach is to use prior assumptions on the flow field in the vessel of

I. Ekroll and J. Avdal are with CIUS and the Department of Circulation and Medical Imaging, Norwegian University of Science and Technology. I. Ekroll is also with St. Olavs hospital HF, Kirurgisk Klinikk

H. Liebgott is with the Université de Lyon, CREATIS; CNRS UMR5220; INSERM U1044; INSA-Lyon; University Lyon 1, 69621 Villeurbanne, France.

V. Perrot was with the Université de Lyon, CREATIS, and is now with the Engineering Physics Department, Polytechnique Montréal, Canada

interest either as a regularization on the estimated flow field [19], [20], or to derive the flow pattern in low flow regions directly from estimates closer to the center of the lumen [21]. This latter approach partially disregards velocity estimates near the wall due to signal loss.

One approach proposed to improve separation between blood and clutter signal in low flow applications is the use of Singular Value Decomposition (SVD) or Eigenvalue decomposition [22], [23]. The use of such filters in quantitative applications, however, is not straightforward as they do not have a well defined frequency response, as is the case for Finite Impulse Response (FIR), Infinite Impulse Response (IIR) and even polynomial regression filters [24]. The lack of a frequency response makes it challenging to predict the performance of SVD filters, both in terms of blood flow detection and the potential impact on estimates of velocity magnitude and direction. The performance of such filters should therefore be assessed separately for each application.

One application in which accurate low flow vector velocity estimates are important, is the estimation of wall shear stress (WSS). WSS is known to influence both the development of atherosclerosis and progression of plaques [25], [26]. Measurements of the WSS, or the purely velocity derived parameter wall shear rate (WSR), could therefore aid in the assessment of progressing vascular disease. However, clinically valuable measurements of the WSR depends on accurate estimates of the magnitude and direction of low velocity blood flow close to the vessel wall, where separation of the blood and clutter signals are particularly challenging.

In this work, we aim to improve the accuracy of vascular vector Doppler estimates in such challenging low flow scenarios. This is achieved by 1) introducing a simulation framework allowing us to mix realistic clutter signal with *in silico* data, enabling assessment of SVD filters on data where the true velocity field is known, 2) assessing the impact of SVD and FIR based clutter filtering techniques on the blood signal, and 3) proposing and assessing the performance of a new method, termed tapered Vector Doppler, to compensate for filtering effects.

The motivation for and description of the tapered Vector Doppler method is included in Section II. Section III provides details on the applied acquisition, processing and generation of synthetic datasets. The behavior of SVD filters in carotid blood flow imaging is investigated in Section IV-A, followed by assessment and validation of the suggested tapering technique in Section IV-B to IV-F. Discussion of results and limitations is included in Section V, before concluding the paper in Section VI.

II. TAPERED VECTOR DOPPLER (TVD)

A. Rationale

In both conventional Color Flow Imaging and Vector Doppler imaging, the mean velocity from each receive beam direction is estimated from the autocorrelation function of the Doppler signal. If $s(k)$ is sample k of the complex signal

after IQ demodulation from a pixel of interest, then the autocorrelation function R of s can be estimated as

$$R(m) = \frac{1}{M-m} \sum_{k=1}^{M-m} s(k)^* s(k+m), \quad (1)$$

where m is the lag and M is the number of samples in the observation window. The phase angle of $R(m)$ for $m \neq 0$ can be used to estimate the axial velocity component of blood [27].

$$\hat{v}_{ax} = \frac{\angle R(m)c \text{PRF}}{4\pi m f_0} \quad (2)$$

where c is the speed of sound, PRF is the pulse repetition frequency and f_0 is the pulse center frequency. In order to remove the signal from tissue scatterers, the Doppler signal s is typically highpass filtered before estimating $R(m)$. However, both FIR filters and SVD filters will potentially also remove the lowest frequency components of the blood signal and thus affect the phase angle estimate. In regions containing high velocity flow, the impact of filtering is less significant. This is because the spectral bandwidth of s typically increases proportionally with the center frequency, and the stopband of the filter becomes narrow compared to the bandwidth.

In regions with low velocity blood flow, however, the entire blood signal frequency band may be contained in the stopband of the filter. The remaining signal after filtering will then essentially be highpass filtered white noise. The autocorrelation estimate of such signals have an expected value around the Nyquist frequency and high variance. For the final vector Doppler estimates, this will yield a strong bias away from zero and a corresponding increase in variance yielding spurious velocity vectors. To correct for this bias and simultaneously lower the variance of low flow vector Doppler estimates, we propose a variation of conventional vector Doppler estimates which we have termed Tapered Vector Doppler (TVD).

B. Formulation

In the suggested Tapered Vector Doppler approach, it is assumed that when some, but not all, signals from different receive directions have low SNR, the blood signal from these directions have frequency content in the stopband. This leads to a bias away from zero combined with increased variance. By adjusting the estimated mean velocity components for the corresponding directions towards zero, both bias and variance of the final vector velocity estimate would be reduced. For the Tapered Vector Doppler approach, this is achieved by multiplying the phase angle estimate by a tapering function.

$$\angle \tilde{R}(1) = \begin{cases} \angle R(1) \sin\left(\frac{\pi |R(1)|}{2 P_n \alpha}\right) & \text{if } \frac{|R(1)|}{P_n} < \alpha \\ \angle R(1) & \text{otherwise} \end{cases} \quad (3)$$

In this work, the angle correction factor as a function of $R(1)$ signal power is a standard cosine tapering window, and is shown in the left panel of Fig. 1. In the right panel, it can be observed that with the chosen tapering function, the standard deviation of the corrected estimate would be approximately constant for the lowest SNR values in the case that the original signal is a sinusoid in noise. For all examples shown in this

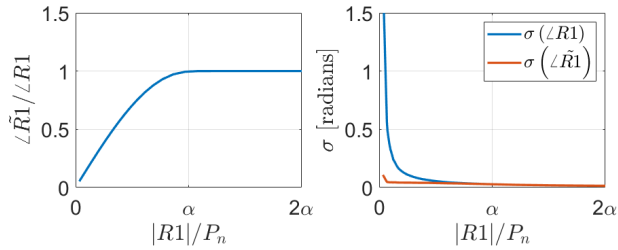


Fig. 1. The left panel shows the proposed angle correction factor used for correction of autocorrelation estimates, using the notation from (5). The right panel shows the impact of tapering on the standard deviation of the corresponding angle estimates, in case of sinusoidal signals in noise.

work, the tapering threshold value $\alpha = 30$, meaning that tapering is applied if the magnitude of $R(1)$ is lower than 30 times that of the noise floor.

C. Alternative tapering methods

The proposed method uses the magnitude of $R(1)$ to determine the tapering factor used to adjust the velocity estimates. An alternative method could be to let the tapering factor depend on $R(0)$ instead. A natural approach would be to set the angle velocity estimate to 0 if the power is below a certain threshold, leading to the formulation:

$$\angle \tilde{R}(1) = \begin{cases} 0 & \text{if } \frac{|R(0)|}{P_n^0} < \alpha_0 \\ \angle R(1) & \text{otherwise.} \end{cases} \quad (4)$$

This method will be referred to as *hard R0 thresholding*. In this work, the parameter $\alpha_0 = 1.5$.

Another alternative is to use the ratio between $|R(1)|$ and $R(0)$ as a discriminator. This ratio is closely connected to the bandwidth of the slow time signal, with values close to 1 associated with high bandwidths, and values close to 0 associated with low bandwidths. This yields the formulation:

$$\angle \tilde{R}(1) = \begin{cases} \angle R(1) \sin\left(\frac{\pi |R(1)|}{2\alpha_R R(0)}\right) & \text{if } \frac{|R(1)|}{R(0)} < \alpha_R \\ \angle R(1) & \text{otherwise.} \end{cases} \quad (5)$$

This method will be referred to as *soft R1/R0 tapering*. In this work, the parameter $\alpha_R = 0.7$.

D. Noise power calculations

To apply tapering, it is necessary to estimate the noise floor P_n or P_n^0 , which are the expected $|R(1)|$ and $R(0)$, respectively, for a signal containing thermal noise only.

In this work the noise floor P_n^0 was calculated as a function of image depth from recordings containing no scatterers. An estimate of P_n is then found by inserting $m = 0, 1$ in (1). For a noise signal, $R(0)$ is the mean of M values that are in phase, whereas $R(1)$ is the mean of $M-1$ complex values with the same expected magnitude, but with random phase. This yields

$$P_n = \frac{1}{\sqrt{M-1}} P_n^0. \quad (6)$$

If it is desirable to apply tapering retrospectively to a recording without access to a noise recording, it is often possible to

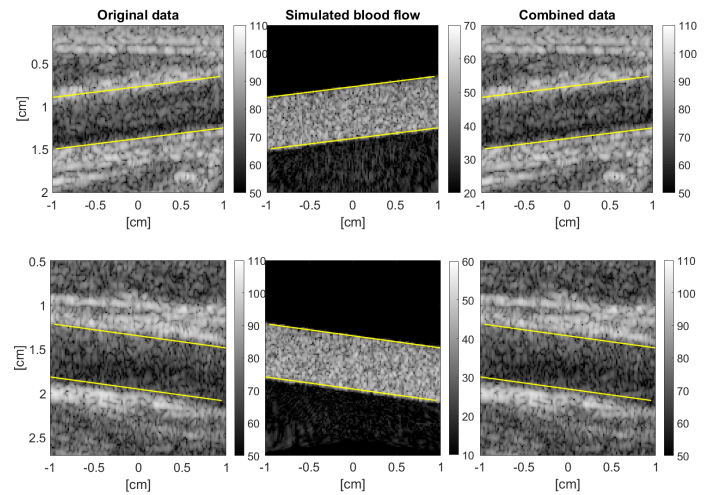


Fig. 2. Single frames from the the original recording (left), the simulated blood flow data (middle), and the combined, synthetic data (right). Upper panels are from the healthy volunteer, lower panels from the patient. SNR and CBR values of 5 and 30 dB were used for the synthetic data,

estimate the spectral noise floor in regions where blood is not covering the entire bandwidth of the Doppler spectrum, and convert this to P_n^0 .

III. METHODS

A. Acquisition

Recordings were performed using a 9L probe (GE Vingmed Ultrasound, Horten, Norway) connected to a Verasonics Vantage 256 channel system (Verasonics Inc., Redmond, WA, USA). Plane wave transmissions (2.5 cycles@4.8 MHz) with alternating insonation angles of $\pm 15^\circ$ were used, resulting in a Doppler PRF of 6 kHz. A multi-angle beamforming scheme was applied on receive [28], enabling robust 2D vector velocity estimation from lag-one autocorrelation velocity estimates.

Two *in vivo* common carotid artery (CCA) recordings were used in combination with flow simulations to create Doppler signals from known velocity fields, influenced by realistic clutter. The first recording was from a 34 year old healthy volunteer, whereas the second recording was from a patient with symptoms of carotid artery disease. The creation of synthetic datasets is described in section III-B. Two additional recordings from a 33 year old and a 66 year old volunteer were used to independently demonstrate the performance of the tapered vector Doppler technique in a realistic imaging setting. Recordings were performed by an experienced clinician, in a study approved by the regional ethical committee.

B. Creation of synthetic datasets

Quantitative assessment of the processing chain based on *in vivo* recordings is difficult as the true blood velocities are not known. In addition, Doppler data containing realistic clutter, including reverberations and sidelobes from moving tissue, is challenging to simulate. To obtain both realistic clutter and a known flow field, synthetic data sets were constructed by combining recorded tissue signal and simulated blood signal. The synthetic data set was produced using 5 steps:

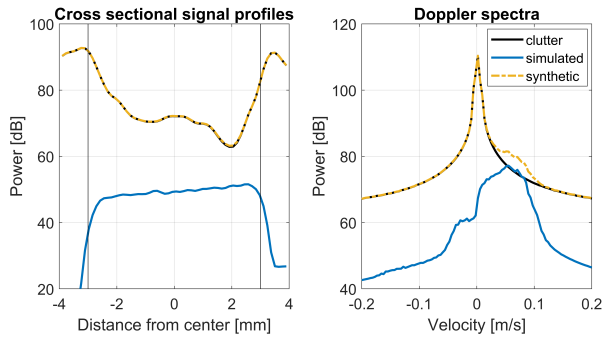


Fig. 3. The left panel shows the average cross sectional signal power in the vessel region for a single frame from the healthy volunteer (broadband clutter scenario). The right panel shows average Doppler spectra of the same signals. The original clutter signal is seen in black, the simulated blood signal in blue, and the combined, synthetic signal in yellow.

- 1) Record *in vivo* data.
- 2) Extract vessel geometry from the common carotid artery, modelling the vessel as a straight tube.
- 3) Simulate flow data with the resulting geometry, using the *in vivo* acquisition and beamforming setup.
- 4) Remove original blood signal from *in vivo* data:
 - Low pass filter
 - Add white noise yielding desired noise floor
- 5) Add simulated blood flow data to yield the desired clutter-to-blood and blood signal-to-noise ratio.

Noise and blood signal were added to the tissue signal after beamforming. The clutter-to-blood ratio (CBR) and blood signal-to-noise ratio (SNR) were estimated by averaging clutter, blood and noise power over the entire lumen.

As indicated in Fig. 2, two 3D vessel regions with diameters of 6 mm were simulated using the Field II software [29], [30], using on average 10 scatterers per resolution cell. Vessel depths and inclinations were based on the *in vivo* geometries. Stationary flow with a parabolic profile was chosen, with a maximum velocity of 20 cm/s in the middle of the artery. The relatively low velocity was selected to mimic challenging parts of the cardiac cycle, where the blood velocity in the artery is low, and the tissue motion is at its largest. A relatively large observation window of 45 ms was used (270 samples), to reduce variance and improve clutter filtering performance.

After subjecting the original data to filtering and addition of noise, the resulting clutter signal was investigated in frequency and eigenvector domains to ensure that no blood signal remained above the noise floor. Simulated blood flow data were then added, creating synthetic Doppler data. Several combinations of luminal SNR and clutter-to-blood ratio (CBR) values were used (Table I). For the healthy volunteer, two observation windows were investigated: one where the clutter was nearly stationary (narrowband clutter), and one including the maximum tissue motion (broadband clutter). For the patient data, the wall motion was less pronounced, and only a single observation window was investigated.

Fig. 3 shows cross sectional signal power (left panel) and Doppler spectra (right panel) from the original clutter signal, simulated blood signal and combined synthetic signal.

TABLE I
ACQUISITION, SYNTHETIC DATA AND PROCESSING PARAMETERS

| Parameter | Value |
|---------------------------------------|----------------------------|
| Transmit frequency [MHz] | 4.8 |
| Pulse cycles | 2.5 |
| Pulse Repetition Frequency [kHz] | 12 |
| Number of transmit angles | 2 |
| Transmit angles [deg] | [-15, 15] |
| Rx angles tx1 [deg] | [-15, -3.5, 6, 15, 0] |
| Rx angles tx2 [deg] | [-6, 3.5, 15, 0] |
| Rx F-number | 1.4 |
| Packet size | 270 |
| Grid resolution | $\lambda/2$ |
| Averaging region complex R1 estimates | $2\lambda \times 2\lambda$ |
| Synthetic blood SNR values [dB] | [0 2 5 8 10] |
| Synthetic CBR values [dB] | [10 30] |
| Velocity profile | Parabolic |
| Maximum velocity [cm/s] | 20 |

The example is from the broadband clutter scenario of the healthy volunteer, with SNR and CBR values of 5 and 30 dB respectively. The figures are obtained using 104 cross-sections normal to the vessel axis, covering the 2 cm long section indicated in Fig. 2.

C. Adaptive clutter filtering

1) *FIR filtering*: Adaptive FIR filtering was performed using a precomputed dictionary of FIR filters to reduce the computational load and computation time. A list of FIR filters was computed using a cutoff from 1 mm/s to 5 cm/s with a discretization step of 0.01 mm/s. Filters are based on an equiripple design with a stopband attenuation of 70 dB and an order of 170, resulting in 100 valid samples in the observation window after filtering. The relatively high filter order was chosen to obtain sufficient stopband attenuation and a narrow transition band, to remove the clutter signal while simultaneously minimizing the loss of signal from low velocity blood flow. For each frame in the observation window, mean axial wall velocity was estimated in all pixels based on the complex autocorrelation of the received signal. A spatial averaging filter with a 2D Hanning kernel of 1 mm was applied to the complex autocorrelation to reduce variance. Then, the filter with cutoff closest to twice the maximum mean axial wall velocity was selected from the dictionary. The factor of two was chosen to ensure that no remaining clutter was present without setting a too high cutoff value.

2) *Adaptive SVD filtering*: Unless otherwise specified, adaptive SVD filtering was applied individually to each Doppler frame. The correlation of spatial eigenvectors was used to automatically determine the dimension of the clutter space, inspired by the work of Baranger et al. [23]. Filtering was performed by removing the corresponding eigenvectors.

D. Vector velocity estimation

2D vector velocities were estimated based on an extended least squares technique (ELS-VD) [28] utilizing multiple lag-one complex autocorrelation estimates. More specifically, the Doppler frequency is estimated for $L = 7$ different transmit-receive (tx/rx) angle combinations, each corresponding to

a unique two-way Doppler angle, yielding the normalized measurement vector

$$\hat{\mathbf{f}} = [\angle R(1)_0 \dots \angle R(1)_L] / \pi. \quad (7)$$

The velocity vector $\mathbf{v} = [v_x, v_z]$ corresponding best to the measured Doppler shifts can then be found by solving a least squares problem. In the general formulation, aliasing is accounted for, yielding separate least squares problems for each aliasing pattern \mathbf{g}_i :

$$k\mathbf{A}\mathbf{v}_i = \hat{\mathbf{f}} + \mathbf{g}_i. \quad (8)$$

Here, k is a constant factor converting velocity to normalized frequency. The matrix $\mathbf{A} = \mathbf{A}_{\text{tx}} + \mathbf{A}_{\text{rx}}$ has dimensions 7×2 , and is the sum of the projection matrices onto the transmit and receive Doppler directions, respectively. The rows of \mathbf{A} are given by $\mathbf{a}_l = [-\sin \alpha_l - \sin \beta_l, \cos \alpha_l + \cos \beta_l]$ where α_l and β_l are the steering angles of the angle pair l on transmit and receive, respectively.

The general solution to these equations are

$$\mathbf{v}_i = k^{-1} \mathbf{A}_{\mathbf{W}}^+ (\hat{\mathbf{f}} + \mathbf{g}_i), \quad (9)$$

where $\mathbf{A}_{\mathbf{W}}^+$ is the weighted pseudoinverse of \mathbf{A} , given by

$$\mathbf{A}_{\mathbf{W}}^+ = (\mathbf{A}^T \mathbf{W} \mathbf{A})^{-1} \mathbf{A}^T \mathbf{W} \quad (10)$$

The diagonal matrix \mathbf{W} in (9) allows for weighting of the individual measurements to account for e.g. variance.

The Tapered Vector Doppler approach will be compared to two other variations of the ELS-VD technique. Differences in the vector velocity estimators are highlighted in the following:

1) *Standard*: In the standard implementation of ELS-VD, $\mathbf{W} = \mathbf{I}$, yielding the solution

$$\mathbf{v}_i = k^{-1} \mathbf{A}^+ (\hat{\mathbf{f}} + \mathbf{g}_i), \quad (11)$$

2) *Weighted least squares*: Two variations of weighted least squares were implemented. In the conventional approach (WLS), weights are inversely proportional to the variance of the $R(1)_l$ phase angle estimates, yielding the following expression for the diagonal elements of \mathbf{W} [27]:

$$w_{l,l} = \frac{1}{2} \left(1 - \frac{|R(1)_l|}{R(0)_l} \right)^{-1} \quad (12)$$

In the alternative approach (WLS-R1), the weights are proportional to the magnitude of $R(1)_l$ squared, that is

$$w_{l,l} = |R(1)_l|^2. \quad (13)$$

In both WLS implementations, the final vector velocity estimates are found using (9) and (10) with the appropriate weighting.

3) *Tapered Vector Doppler*: As detailed in Section II, tapering accounts for filter attenuation by modifying the Doppler measurement vector in (7) to

$$\tilde{\mathbf{f}} = [\angle \tilde{R}(1)_0 \dots \angle \tilde{R}(1)_L] / \pi, \quad (14)$$

yielding the modified solution

$$\mathbf{v}_i = k^{-1} \mathbf{A}^+ (\tilde{\mathbf{f}} + \mathbf{g}_i), \quad (15)$$

For all approaches, complex autocorrelation estimates are averaged in a 4×4 pixel region defined by the beamforming grid (see Table I). No regularization or filtering is applied to the vector velocity estimates.

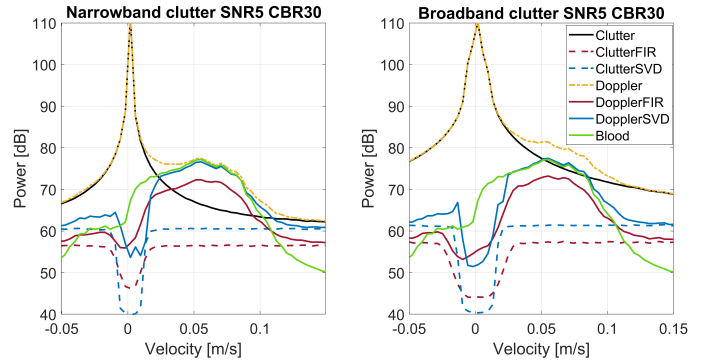


Fig. 4. Filter impact on the synthetic Doppler signal (yellow) and clutter signal only (black). Red color is used in the case of FIR filtering, and blue color in the case of SVD filtering. The dashed lines show the frequency content of the remaining signal after applying the filters on the clutter signal alone, whereas the continuous red and blue lines show the synthetic signal after FIR and SVD filtering respectively. The green line shows the blood signal before filtering. The power estimates were produced by averaging power spectra from every image point within the vessel region before and after applying the adaptive filters.

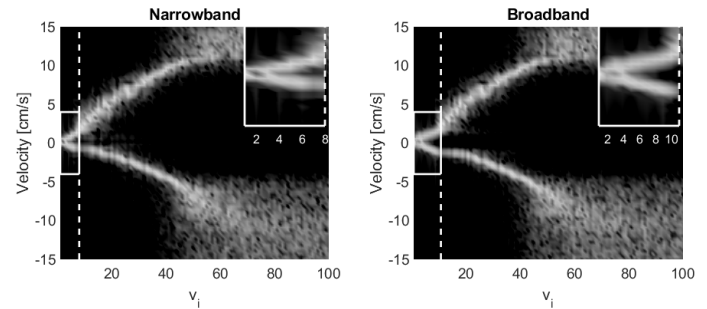


Fig. 5. Eigenvector spectra from the narrowband (left) and broadband (right) clutter scenarios. The panel insets zoom in on the region determined to represent the clutter signal in the SVD filtering process. The spectra are based on the synthetic signals shown in yellow in Fig. 4. Only the first 100 eigenvectors are included in the figure. The remaining 170 contain noise.

E. Wall shear rate estimation

As further quantitative assessment of the tapered Vector Doppler method, wall shear rate was estimated from the synthetic blood flow data. After vector Doppler estimation, velocity estimates were reinterpolated to a grid parallel to the vessel walls. If (x, z) denotes an image point close to the vessel wall, the wall shear rate is calculated as

$$\gamma(x, z) = \frac{\partial v_x}{\partial z} + \frac{\partial v_z}{\partial x}. \quad (16)$$

The spatial derivatives were calculated using numerical differentiation with a spatial lag of 0.6 mm. The wall shear rate associated with a spatial position in the wall was then defined as the largest value of γ observed within 1 mm from the wall along a line in the radial direction.

IV. RESULTS

A. Clutter filtering in low flow scenarios

FIR filters have a well defined frequency response, and will predictably attenuate blood signal with frequency content below the filter frequency cut-off. Decomposition of the signal

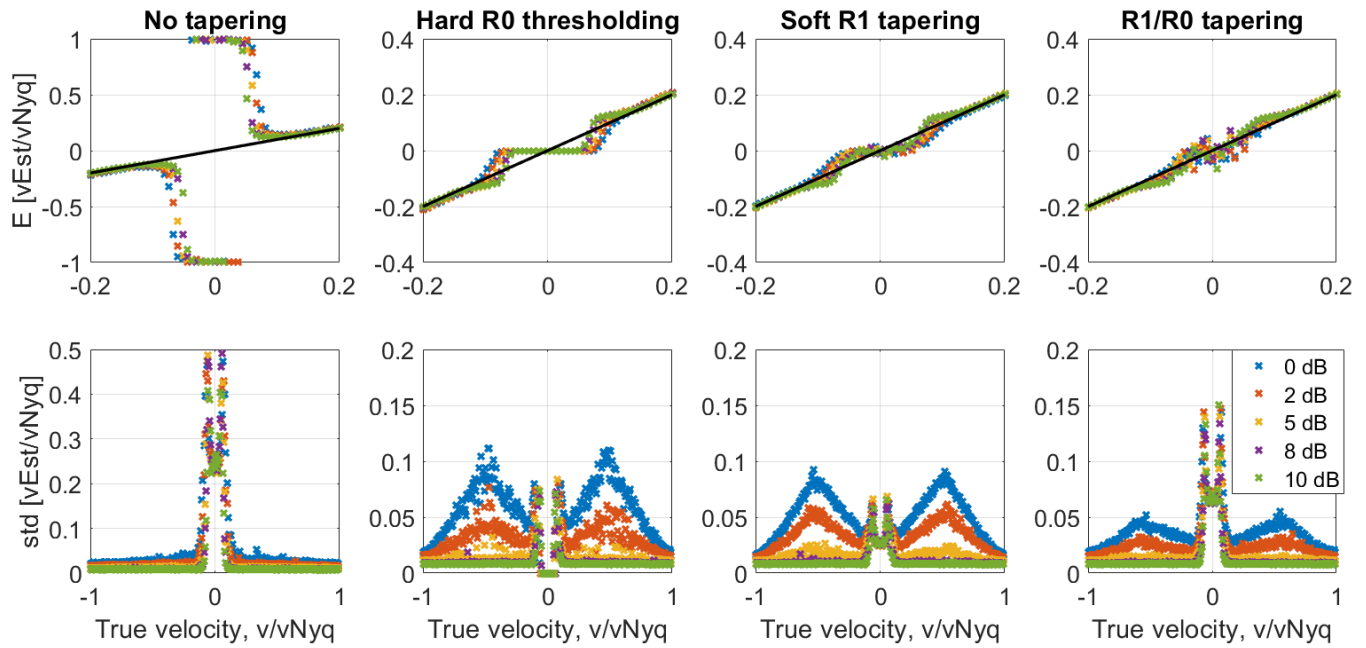


Fig. 6. Mean velocity estimates normalized by the Nyquist velocity without tapering and using different tapering techniques. In the region around zero velocity, the clutter filter results in mean velocity estimates with high variance and bias. The use of tapering ensures that these highly erroneous estimates are placed around zero.

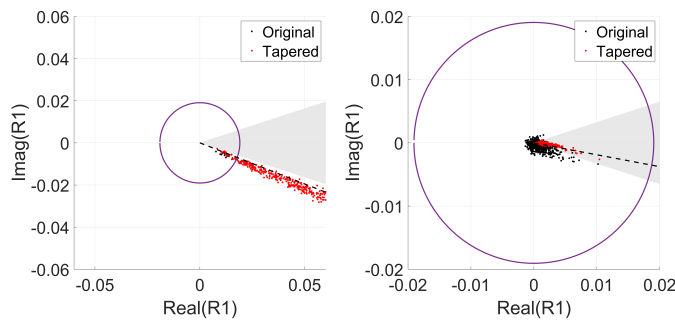


Fig. 7. $R(1)$ estimates based on 500 realizations of a single velocity with average SNR 10 dB. Ideally, the $R(1)$ estimates should be located along the dashed, black line, indicating the true velocity. In the right panel the velocity is within the filter stopband, depicted in gray. The circle corresponds to the power threshold below which tapering is applied. Without tapering, the angular distribution of $R(1)$ deviates significantly from the true velocity line, whereas the use of tapering yields improved alignment.

into its eigencomponents will in general not be equivalent to a frequency decomposition, and the impact of SVD filtering on the frequency content of the signal is therefore less predictable. This motivated a comparison between SVD filters and adaptive FIR filters with regard to their impact on the frequency content of the signal in this application.

A typical example of the impact of the two investigated filter types is shown in Fig. 4. The left and right panels show Doppler velocity spectra from the synthetic data sets with narrowband and broadband clutter respectively. Also shown is the impact of the clutter filters on the clutter signal alone (dashed lines). It can be observed that both the FIR and SVD filter adapt to the changing clutter motion by varying the stopband region around zero velocity, with some differences

in attenuation of the lowest velocities and sharpness of the transition region.

Fig. 5 shows the frequency content (converted to velocity) of the temporal eigenvectors of the luminal signal in the narrow- and broadband clutter scenario. The white, dashed line shows the filter threshold found using correlation of the spatial eigenvectors. In both cases, the power spectrum is approximately symmetric and narrowband prior to the threshold value, and removing the eigencomponents prior to the threshold value will also remove the lowest frequency components of the blood signal.

The examples shown are representative for all investigated data frames, indicating that for the current application and processing, SVD filtering still behaves similarly to a frequency based filter. It will therefore also share the limitations of frequency based filters in a low flow scenario, namely that they cannot separate blood flow and clutter yielding similar Doppler shifts.

B. Numerical simulations

Simple numerical simulations of Doppler signals were used to illustrate the effect of tapering on Doppler angle estimates. Fig. 6 shows Doppler axial velocity estimates as a function of true axial velocity for different tapering methods and a range of SNR values. The bandwidth of the Doppler signals were 6 % and the filter stopband width was 4% of the sampling frequency. Using a packet size of 270 and a 170 order FIR filter yields 100 samples for averaging before determining the phase of the lag one autocorrelation estimate. For each velocity bin, the marker represents the mean value of 500 realizations. As may be observed, the mean velocity estimates without tapering suffer from both significant bias and high variance within the

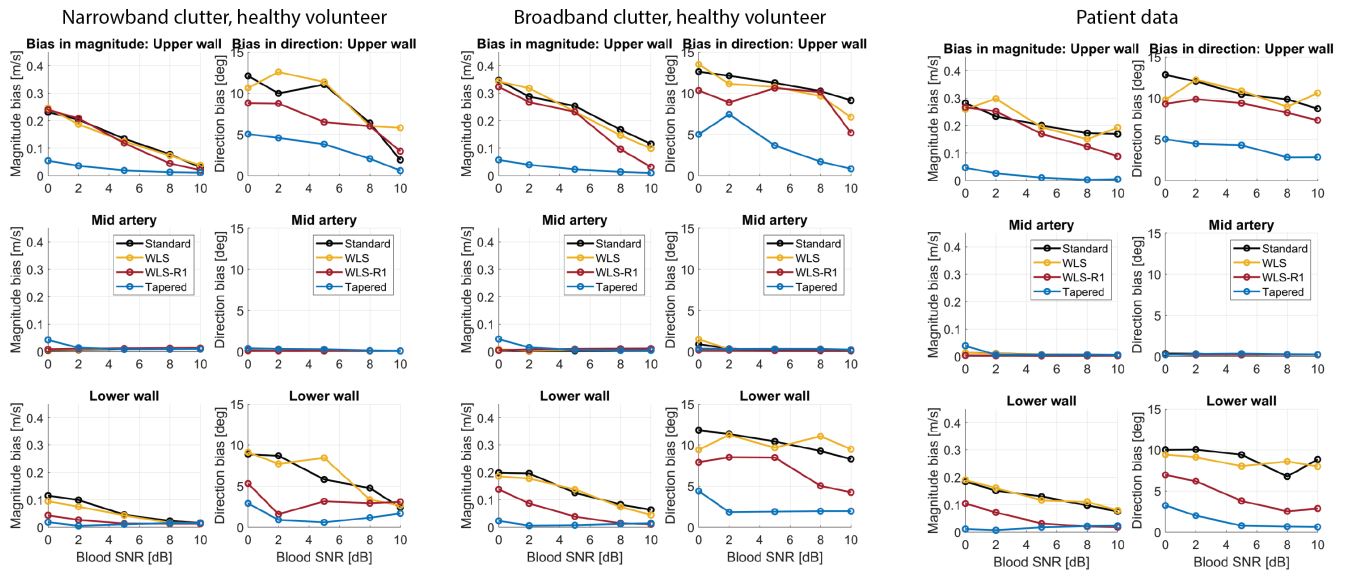


Fig. 8. Bias in velocity magnitude (left columns) and direction (right columns) for all synthetic datasets as a function of SNR. The CBR is 30 dB. The arteries are subdivided into three sections based on distance from the vessel axis. Upper wall (-3 mm - -1 mm), mid artery (-1 mm - 1 mm) and lower wall (1 mm - 3 mm). Each measurement point is formed by calculating the RMS value of the bias over all valid points in 104 cross sections.

filter stopband. This bias is largely corrected for by using tapering. Of the evaluated tapering methods, soft $R(1)$ tapering exhibits the lowest variance for low velocities, and also avoids the steep transition towards zero velocity seen when using hard $R(0)$ thresholding. In subsequent results, tapering will refer to soft $R(1)$ tapering unless otherwise specified.

Fig. 7 further illustrates the effect of tapering, showing complex $R(1)$ estimates from all 500 realizations for two single velocities. The angle corresponding to the true velocity is shown as a black, dashed line. The left panel shows a case where the true velocity is right outside the filter stopband. Most $R(1)$ estimates have magnitude larger than the tapering limit and are not adjusted. In the right panel, the velocity is within the filter stopband, causing significant attenuation of the blood signal, with corresponding low values of the $R(1)$ magnitude. It can be observed that whereas the original $R(1)$ estimates have a widespread angular distribution, tapering yields a distribution of $R(1)$ values in good agreement with the true velocity.

C. Quantitative analysis on synthetic data

Fig. 8 shows the bias in the vector velocity estimates of all three synthetic data sets, for the investigated SNR scenarios. The vessel is subdivided into three regions of interest: 1) close to the upper wall, 2) mid artery and 3) close to the lower wall. This is done to enable inspection of the low velocity regions specifically, and also highlight differences due to reverberations and the point spread function. The use of tapering decreases the bias both in velocity direction and magnitude compared to the standard ELS-VD and WLS approaches. The largest improvement is seen close to the upper wall. In this region the average blood velocity was 9 cm/s, and for 5 dB SNR the use of tapering lead to a reduction in bias from 26.3 cm/s to 1.4 cm/s.

Fig. 9 shows estimated velocity profiles from synthetic data based on the patient recording. The results illustrate that filtering using SVD or FIR filters removes low velocity blood flow close to the vessel wall, yielding velocity estimates with high standard deviation. The suggested tapering approach yields reduced bias and variance in the vector velocity estimates compared with the standard and WLS variations of ELS-VD. Although the estimates of velocity magnitude and direction both show reduced bias and variance, the most significant improvement in performance is seen in the estimates of velocity magnitude. The lower panels show the normalized $R(1)$ magnitude and the standard deviation of $R(1)$ phase angle estimates from each tx/rx direction. The corresponding $R(1)$ phase angle estimates are shown in Fig. 10. The two receive directions that are most affected by tapering are those with the lowest true axial velocity components. Without tapering, the corresponding velocity component estimates are significantly overestimated. The use of tapering in this case reduces the bias in the regions with high variance near the vessel walls.

Fig.11 shows the mean and standard deviation of the estimated velocity magnitude mid vessel and in the vicinity of the upper wall with and without tapering. The left panels show velocity magnitude estimates as a function of removed clutter components when applying SVD filtering, whereas the right panels show velocity magnitude estimates as a function of FIR filter velocity cutoff value. Estimates of mean and standard deviation are based on 104 values at the same distance from the vessel axis. The relation between estimated velocity magnitude and filter strength when no tapering is applied is shown in gray. When using SVD filtering, a strong initial transient is present, associated with the removal of an increasing amount of clutter signal. After a more stable level where the estimates are dominated by signal from blood flow, a second transient region follows as the signals become increasingly dominated

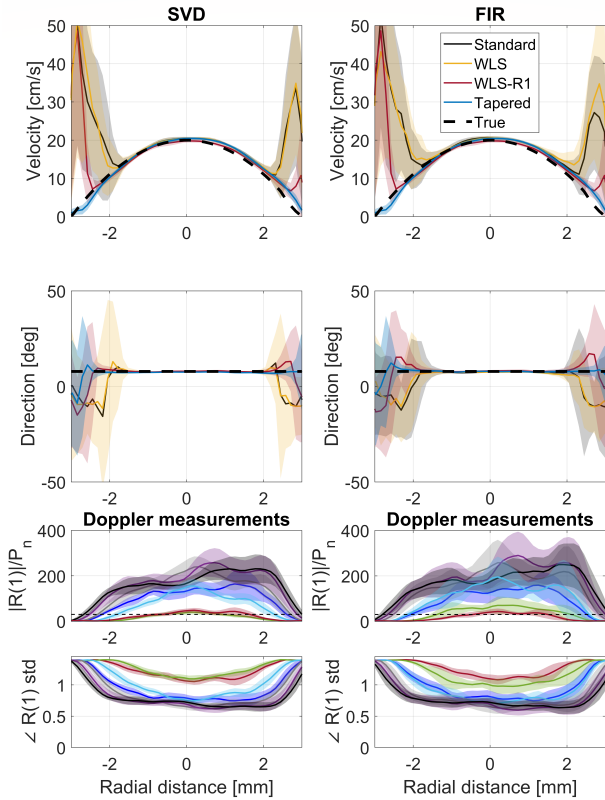


Fig. 9. Velocity profiles from the patient dataset using standard ELS-VD (black), WLS (yellow and red) and TVD with soft R1 tapering (blue). In the left and right panels, clutter suppression is performed using SVD and FIR filtering respectively. CBR and SNR values are 30 dB and 5 dB. The lower panels show, for each of the 7 receive directions, mean and standard deviations of quantities used for tapering and weighted least squares: the ratio between $|R(1)|$ and the noise floor, and the standard deviation of $R(1)$ angle estimates. Horizontal dashed lines denote the power level below which tapering is gradually applied.

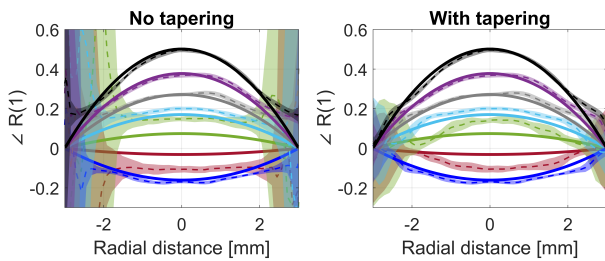


Fig. 10. Mean and standard deviation of $R(1)$ phase angle estimates, with and without tapering, for the seven different Doppler receive directions, corresponding to the velocity estimates using SVD filtering in Fig. 9. Solid lines denote the ground truth velocity components.

by noise, resulting in rapidly increasing velocity magnitudes. It should be noted that when tapering is applied, the region around the chosen cutoff-value has more stable velocity estimates, and a significantly lowered variance as compared to the standard case with no tapering. In the vicinity of the vessel wall, tapering also leads to a significant decrease in velocity bias compared to the standard no-tapering case.

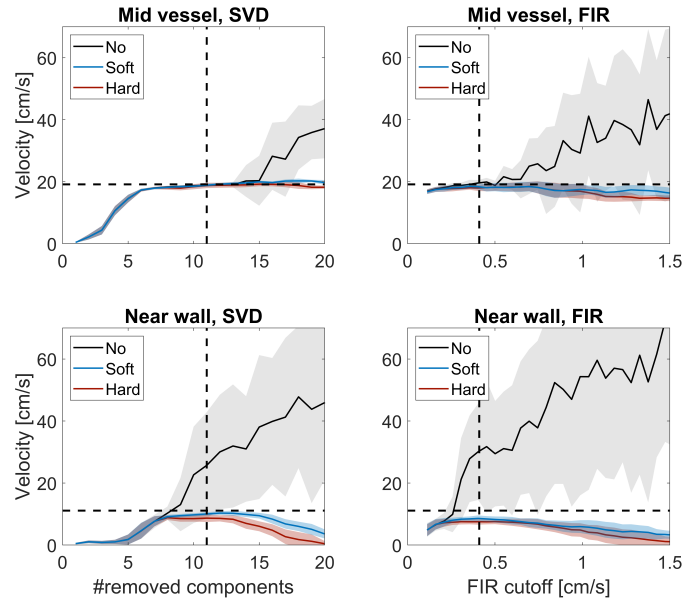


Fig. 11. Estimated velocity magnitude as a function of filter cutoff values when using SVD (left) and FIR (right) in the synthetic data with broadband clutter. The horizontal dashed line indicate true velocity, whereas the vertical dashed line indicates the automatically chosen cutoff-value for the SVD and FIR filters. Mean and standard deviations are shown for standard ELS-VD (black), TVD with soft R1 tapering (blue) and ELS-VD with hard R0 thresholding (red). CBR and SNR values are 30 dB and 5 dB.

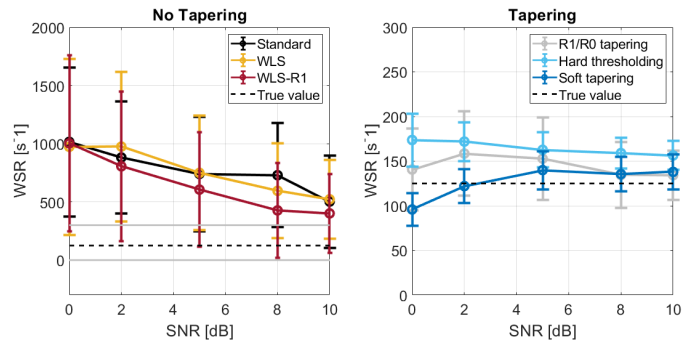


Fig. 12. Wall shear rate estimates for a range of SNR values. The left panel shows results using the standard and WLS versions of ELS-VD, whereas the right panel shows the results using different tapering approaches. The true WSR value is shown as a dashed, black line. Notice the large difference in WSR axis limits, also indicated by the gray horizontal lines in the left panel.

Wall shear rate estimates with and without tapering are shown in Fig. 12. As can be observed, the estimators using both hard $R(0)$ thresholding and soft $R(1)$ tapering yield much more accurate wall shear rate measurements than standard Vector Doppler and weighted least squares Vector Doppler. Of these two alternatives, soft $R(1)$ tapering provided more accurate estimates, with a bias below 10% for all measured SNRs. In comparison, the WSR when using hard $R(0)$ thresholding was overestimated by 22-38%.

D. In vivo data processing: Computational load

The computational load of critical steps in the processing chain are summarized in Table II. Implementations have not

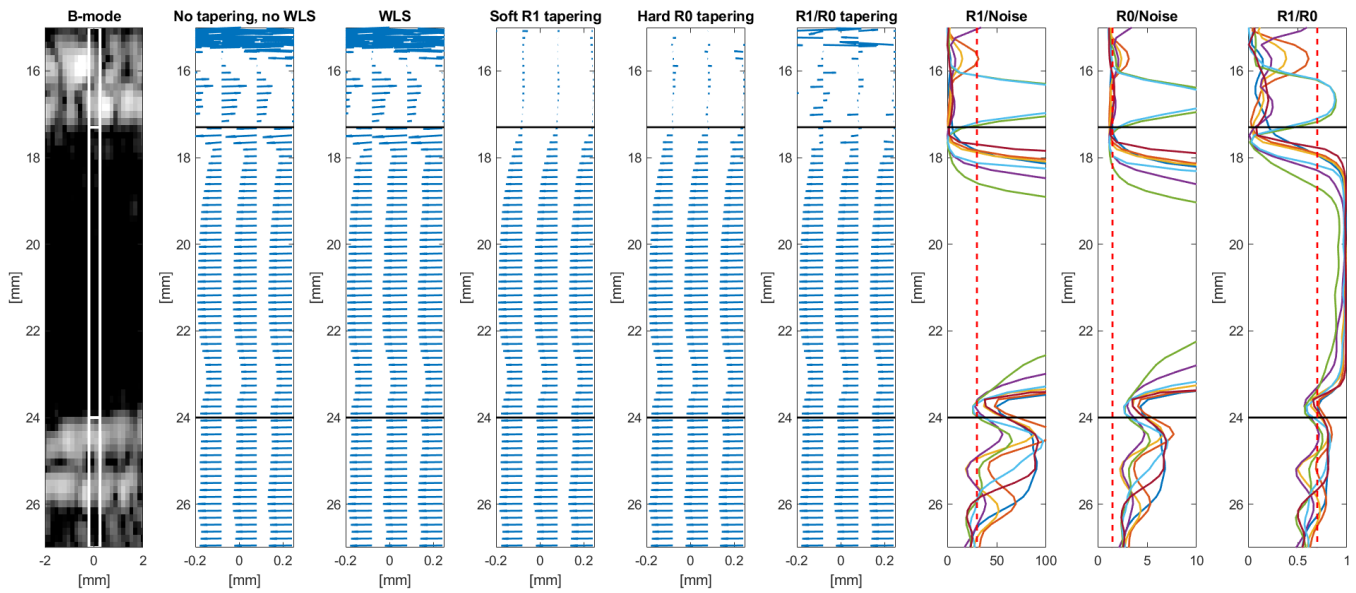


Fig. 13. Example of regular and tapered vector Doppler in diastole of a 66 year old volunteer. All vector velocity estimates shown are from the region indicated by white lines in the left panel. Differences are seen close to the upper wall, where filtering has suppressed the blood signal. Close to the lower wall, sidelobes from mid-vessel blood flow with high velocities yield higher SNR after clutter filtering and therefore smaller differences between regular and tapered VD.

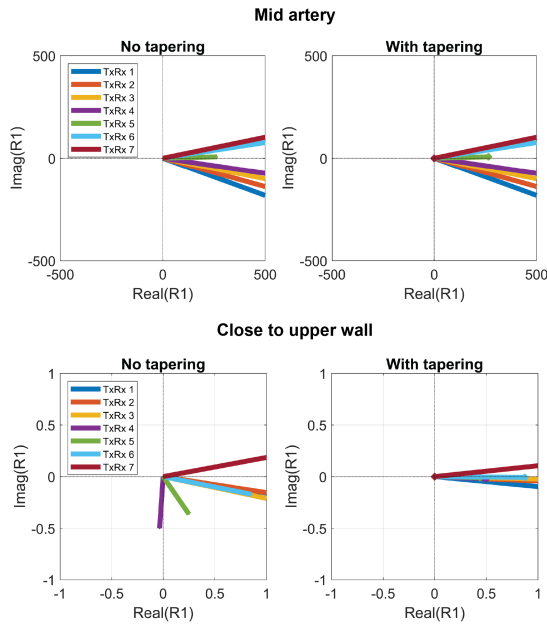


Fig. 14. Estimates of $R(1)$ for each transmit/receive direction for a voxel in the middle of the artery (top panels), and close to the upper wall (bottom panels) in the frame shown in Fig. 13. Note the difference in axes limits.

been parallelized or optimized for speed, but processing times are still reported to give an impression of the potential for future real time implementation. The reported times are for processing 90, 270 and 2000 frames in a Matlab environment, each frame consisting of 158×274 beamformed pixels and 7 receive directions, on a 2.1GHz Intel Xeon CPU with 128 GB RAM available.

TABLE II
PROCESSING TIME CRITICAL STEPS

| | 90 frames | 270 frames | 2000 frames |
|---------------------|-----------|------------|-------------|
| Beamforming | 9.2 s | 22 s | 162 s |
| SVD calculation | 0.27 s | 0.9 s | 29 s |
| Non-tapered Doppler | 1.14 s | 1.23 s | N/A |
| Tapered Doppler | 1.14 s | 1.24 s | N/A |

E. In vivo example: Common carotid artery

Fig. 13 demonstrates the difference between regular and tapered least squares vector Doppler for diastolic flow in the common carotid artery of the 66 year old volunteer. The impact of the clutter filter and subsequent tapering is most significant close to the upper wall. This is further illustrated in Fig. 14, which shows $R(1)$ estimates from all TxRx directions for two points in the artery. In the middle of the artery, the blood signal was not significantly affected by the clutter filter, yielding an SNR between 7 and 15 dB for the different TxRx directions, and no tapering of the $R(1)$ estimates. Close to the upper wall, however, the blood signal was highly attenuated by the clutter filter, yielding a low SNR and a wider angular distribution. It can be observed that estimates from TxRx 4 and 5 are especially affected, and biased towards the Nyquist limit. The use of tapering adjusts the angular distribution of the $R(1)$ estimates, yielding a more reasonable flow field.

F. In vivo example: Complex flow in the carotid bifurcation

Fig. 15 shows estimated vector velocities with and without tapering, and also when removing 60% of automatically selected eigencomponents. The selected frames are from systolic upstroke and diastole, whereas the supplementary videos capture the full lifespan of the recirculation zone (vortex) in the

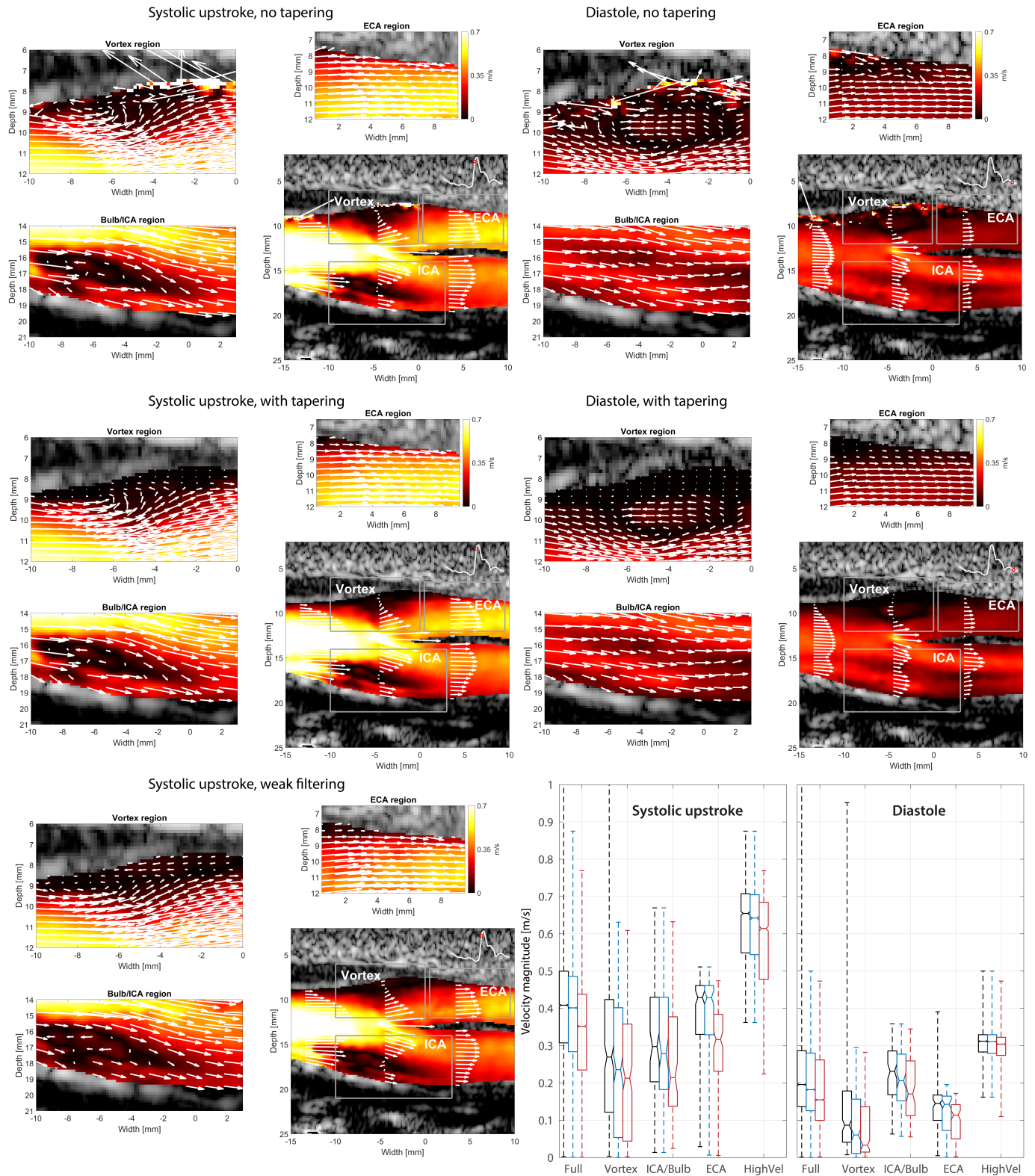


Fig. 15. Left panels show the estimated flow field in the carotid bifurcation during systolic upstroke: Regular SVD filter + standard ELS-VD (top), regular SVD filter + TVD (middle) and weak (60%) SVD filtering + standard ELS-VD (bottom). Vector flow images in the right panels show the estimated flow field in a diastolic frame using regular SVD filtering with (middle) and without (top) tapering. The bottom right figure summarizes statistics for the whole bifurcation flow field and the smaller regions of interest. The line in the middle of the boxes represent the median value of the velocity magnitude, whereas the bottom and top of each box are the 25th and 75th percentiles, respectively. The whiskers include all remaining velocity estimates in each region. Standard ELS-VD is shown using black boxes, TVD is shown using blue boxes, whereas weak filtering + ELS-VD is shown in red boxes. No regularization has been applied to the vector velocity fields. See also supplementary videos capturing flow throughout the cardiac cycle.

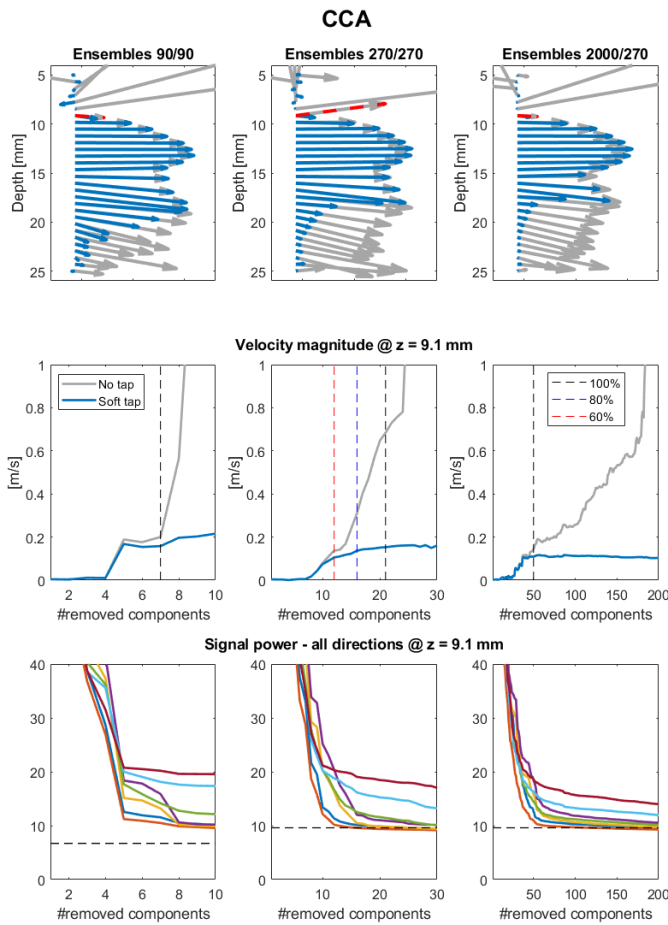


Fig. 16. Top panels show estimated velocity vectors during systolic upstroke, for a cross-section in the CCA, and for different combinations of filter observation window and Doppler ensemble size. Note that the filter observation window is longer than the Doppler ensemble size in the rightmost column. Middle panels show the magnitude of the velocity estimate in a single grid point near the wall, for varying numbers of removed eigencomponents. Lower panels show the power of the signals from different receive directions after filtering. The dashed horizontal line denotes the noise floor. Supplementary videos show the associated flow fields with and without tapering.

upper part of the bifurcation. When using the automatically selected SVD filter order without tapering, spurious velocity estimates are observed near the upper walls.

The boxplots in the lower right panels of Fig. 15 provide summary statistics for the estimated flow field in the whole bifurcation region, in addition to some smaller regions of interest. It can be observed that the velocity magnitudes are in general lower when using a weaker SVD filter (red boxes), particularly during systolic upstroke and in the external carotid artery. The effect of tapering is seen by comparing the blue and black boxes. Differences are particularly evident in the vortex region, where the top whiskers has a significantly reduced length when tapering is applied. This corresponds to the lack of spurious vectors with high velocity magnitude seen in the vector velocity images.

Fig. 16 shows how the number of removed eigencomponents impacts velocity magnitude estimates in a low flow region in the CCA. The lower panels show signal power after filtering for each of the 7 receive directions. Results are shown for

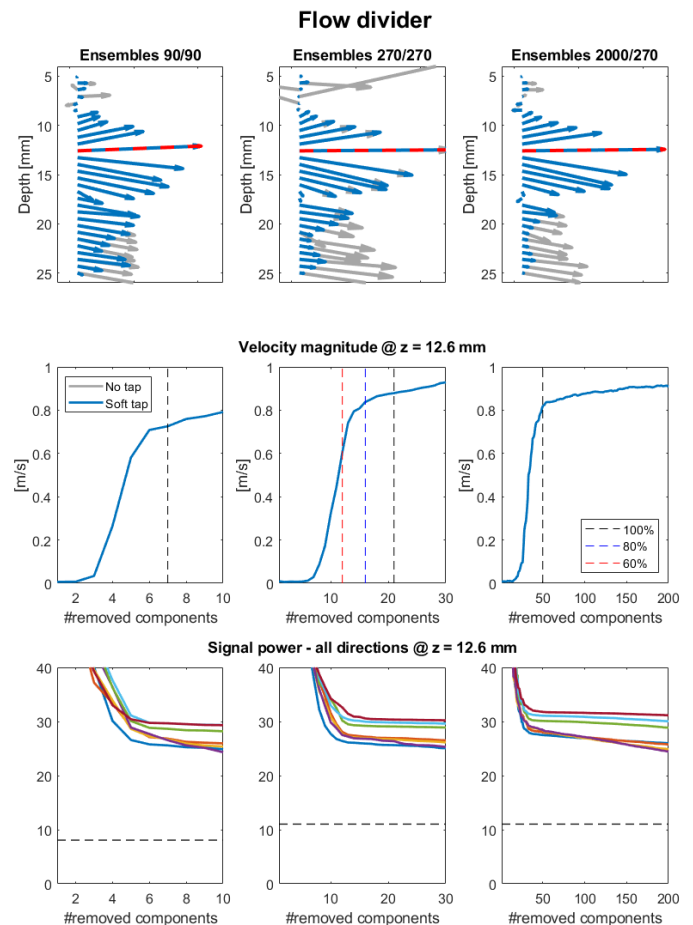


Fig. 17. Top panels show estimated velocity vectors during systolic upstroke, for a cross-section in the high velocity region before the flow divider, and for different combinations of filter observation window and Doppler ensemble size. Note that the filter observation window is longer than the Doppler ensemble size in the rightmost column. Middle panels show the magnitude of the velocity estimate in a single grid point close to the flow divider, for varying numbers of removed eigencomponents. Lower panels show the power of the signals from different receive directions after filtering. The dashed horizontal line denotes the noise floor.

three combinations of filter observation windows and packet sizes. As can be observed in the middle panels, the estimated velocity magnitudes are largely dependent on the number of removed eigencomponents. When using tapering, the velocity estimates eventually reach a plateau. When not using tapering, however, only a small range of filter parameters yields stable velocity magnitudes. These observations correspond well with near wall estimates from synthetic data shown in the lower left panel of Fig. 11.

Fig. 17 shows the corresponding results from a high velocity region in the same temporal frame. In this region, the signal power is significantly higher than the noise floor, and estimates with and without tapering are identical. Also, velocity magnitudes both with and without tapering stabilize after removing enough eigenvectors.

Fig. 18 shows a comparison between velocity profiles obtained using tapering and those obtained without tapering, but using a lower number of removed eigencomponents. The results indicate that velocity estimates are sensitive to clutter filter

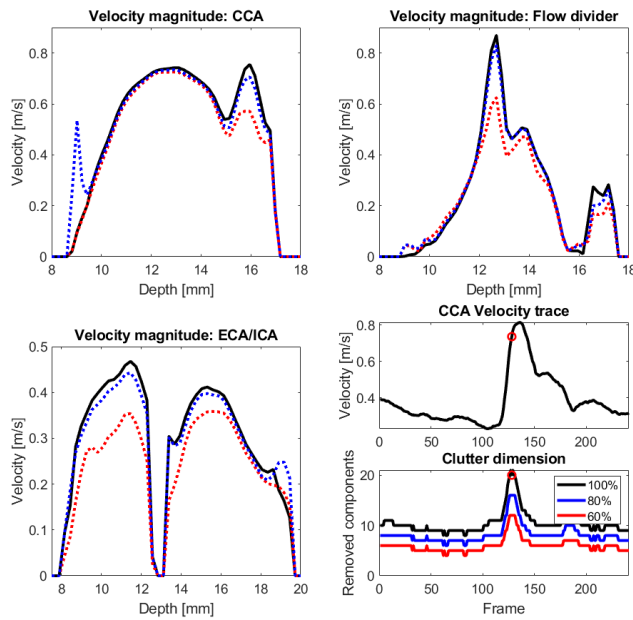


Fig. 18. Top and middle panels show vector velocity estimates in the CCA and ECA/ICA cross sections indicated in the left panels of Fig. 15. TVD estimates following the adaptive SVD filtering is shown in black. Results after applying SVD filters removing 80% and 60% as many eigencomponents, but without tapering are shown in blue and red respectively. The bottom panels shows a CCA velocity trace with the inspected frame (left), and the applied SVD clutter dimension as a function of frame number (right).

strength along the upper and lower walls in the CCA, and throughout the lumen in the ECA and ICA.

V. DISCUSSION

An approach for improving the accuracy and robustness of vector velocity estimation of low flow in the carotid arteries has been proposed. First, it was shown that for the relevant setup and application, SVD and adaptive FIR filters shared some of the same limitations in separating low velocity blood signal from moving tissue signal. To address these limitations, a tapered Vector Doppler technique was proposed, in which signal loss after clutter suppression is used to indicate Doppler measurements where the blood signal is in the stopband-region of the filter. Synthetic data created using a combination of *in vivo* data and flow simulations were used to show that the proposed method reduces bias and variance in the resulting vector velocity estimates compared to standard and weighted-least squares vector Doppler implementations. Promising results were also shown *in vivo* using recordings from healthy volunteers.

FIR and SVD filtering

In Fig. 4, it is demonstrated that both SVD and FIR filters are able to adjust the effective frequency response when the tissue signal bandwidth increases. Whereas for the FIR filter this would imply also the loss of low velocity blood signal, ideally for the SVD filter some blood signal would remain with the same frequency content as the tissue signal. The spectra in Fig. 5, however, indicate that, for the current application and

setup, the eigenvector decomposition also essentially behaves like a frequency filter in the low frequency region. This implies that the use of either filtering method to remove tissue signal could result in the removal of low frequency blood components from the Doppler signals. For low velocity blood flow this may lead to significant bias and variance in the corresponding velocity component estimates. The proposed tapering method is an attempt to address this problem.

Although the SVD filter essentially behaves as a frequency filter in this application, it has some other advantages compared to the adaptive FIR filter. As can be seen in Fig. 4, SVD filtering results in a narrower transition band in the frequency domain compared to the FIR filters. In addition, no initialization is necessary for the filter, resulting in a better tradeoff between SNR and temporal resolution.

Design choices

Different tapering approaches were initially evaluated, using either $R(1)$ or $R(0)$, soft tapering or hard thresholding. Of the investigated methods, soft $R(1)$ tapering was the preferred alternative, as it yielded the lowest variance for low velocities. In Fig. 12 it was also observed that the use of hard $R(0)$ thresholding yielded a consistent overestimation of wall shear rate. This corresponds well with the more significant underestimation observed using this method in Fig. 6 and Fig. 11.

In this work, a cosine tapering function with a corresponding parameter $\alpha = 30$ was used to compensate for the increased bias and variance observed when Doppler signals become dominated by noise after filtering. In Fig. 1, it is shown that this choice of tapering function yields approximately constant standard deviation in the complex autocorrelation estimates for narrowband signals. Results from synthetic data in Fig. 9 and Fig. 10 indeed show that low $R(1)$ magnitude is associated with blood signal in the filter stopband and corresponding overestimation of velocity components. The use of tapering in this case yields reduced bias and significantly reduced standard deviation. Some residual bias is observed for receive directions with true axial velocities in the stopband of the clutter filter. This is also predicted by results shown from simulated data in Fig. 6. So although results presented in this work are promising, other tapering functions may be designed to potentially further improve estimates for the relevant application. One such possibility would be to use a function which minimizes bias also for the lowest velocities. But this would probably come at the cost of higher variance. In principle, the tapering function may be optimized based on measured data, e.g. by first estimating the bandwidth and SNR of the blood signal.

Comparison to weighted least squares

Results in Fig. 8, Fig. 9 and Fig. 12 show that the weighted least squares methods were not as effective as tapering methods for reducing bias and variance. The standard WLS approach, using weights inversely proportional to the variance of the angle estimates, arguably did not perform better than ordinary least squares for low velocity flow. Using $|R(1)|$ weights that lead to stronger suppression of unreliable

estimates yielded slightly better results, although a significant bias was still observed for low velocities and low SNR values. There are at least two factors partially explaining this. First, the variance of each R(1) phase angle estimate is typically high, so even though variance is higher for signals dominated by noise, the ratio is not significant enough to suppress the unreliable estimates using standard WLS. This is illustrated in the lower panels of Fig. 9, as the standard deviations of R(1) phase angle estimates only span the range [0.6, 1.4]. Second, the use of WLS implicitly assumes that the velocity component estimates from different directions are unbiased, whereas tapering assumes that phase estimates from signals with very low R(1) magnitude have a bias away from zero. In the current application, the latter assumption is true and this should improve the performance of a tapering approach compared to both WLS methods.

Tapering for robust and accurate velocity estimation

Figure 11 illustrates the relation between velocity estimates and filter parameters. For SVD filters, when removing a low number of eigencomponents, the resulting velocity magnitudes are underestimated. In the middle of the vessel, when increasing the number of removed eigencomponents, the velocity magnitudes reach a plateau with level corresponding well with the true blood velocity. This may be explained by the difference in magnitude between eigencomponents dominated by clutter and blood. The clutter signal is largely contained in a small number of eigencomponents with high magnitude, and each removed clutter signal component has a large impact on the resulting velocity estimate. The signal from blood, on the other hand, tends to be distributed over a larger number of eigencomponents with more uniform magnitude, reducing the impact of each removed eigencomponent on the mean velocity estimates.

When not using tapering, significant overestimation combined with increased variance is observed when removing many eigencomponents. This may be explained by near complete removal of blood signal from at least one of the receive directions, leaving a noise signal with mean frequency around the Nyquist limit and corresponding high variance. This would also explain why overestimation occurs for a lower number of removed eigenvectors in the low flow region near the wall, as the bandwidth of the blood signal is lower. In this region, the estimated velocity magnitude becomes a steadily increasing function of the number of removed components, without any apparent plateau region. The use of tapering, however, removes the observed overestimation, retaining a near unbiased estimate for a higher number of removed eigencomponents. Consequently, the range of removed eigencomponents yielding near correct velocity magnitudes is extended significantly. Results in the right panels show that the above observations are largely valid also for FIR filters, with the filter cutoff serving the same role as the number of removed eigencomponents.

In vivo observations

Vector velocity estimates from the carotid bifurcation shown in Fig. 15 show that velocity estimates with and without

applied tapering agree in large parts of the vessels. The main differences are observed in near-wall regions, where spurious estimates are present when not using tapering. As can be seen in the lower left panel, spurious vector velocity estimates may also be avoided by using a weaker SVD filter, i.e. removing a lower number of eigencomponents. However, as shown in the lower right panel, using weaker filters results in lower estimated velocity magnitudes, particularly during systolic upstroke, for which wall movement is most significant.

Fig. 16 and Fig. 17 together illustrate that achieving accurate velocity estimation throughout the image can be challenging without the use of tapering. In the middle panel of Fig. 16, it may be observed that velocity levels in the CCA stabilize when removing 60% of the selected eigencomponents, just before the signal reaches the noise floor level. Removing 80% of eigenvectors would result in increased velocity magnitudes, because signals from several angles are below the noise floor. As observed in Fig. 17, however, removing 60% of eigencomponents results in velocity estimates in the first transient region for the high velocity region close to the flow divider. In these transient regions, small changes in filtering parameters yield a relatively large change in estimated velocity magnitude. Further, based on the observations in Fig. 11, the first transient region is arguably associated with residual clutter and underestimation of velocity magnitudes. Because the results shown in Fig. 16 and Fig. 17 are from the same temporal frame, this would motivate the removal of a different number of eigencomponents for different spatial points, unless tapering is applied. This challenge is also highlighted in Fig. 18. Removing 60% of eigencomponents arguably yields residual clutter signal, whereas removing 80% yields spurious estimates near the upper wall of the CCA. The use of tapering yields results agreeing with the stronger filter in the middle of the vessel, while avoiding spurious estimates along the wall.

The sensitivity of estimated velocity magnitudes on filter parameters seems to decrease with higher filter observation length. This can be observed by studying the slope of the curves in the middle row of Fig. 16. Thus, if not using tapering, one way to reduce the adverse effects of clutter filtering might be to use longer observation windows for the filter, if this is possible for the application of interest. Note that the ensemble size may be shorter than the filter observation window, meaning that it is possible to achieve both high temporal resolution and long temporal windows for filtering. The length of the filter observation window will then determine a trade-off between filter performance and real time feasibility, as shown in Table II.

The severity of underestimation when applying too weak clutter filters will depend on the signal intensity and motion of the wall, and can be challenging to correct for. However, as shown in Fig. 11 and indicated in Fig. 16 and Fig. 17, the use of tapering facilitates the use of stronger clutter filters without the associated bias and variance. Due to the use of many receive beams with a relatively large angle span, accurate velocity estimates can still be produced even though the blood signal is removed from the received signals with beam-to-flow angles close to 90°. For more qualitative applications, using weaker clutter filters could be an option as the presence of

residual clutter will regularize the signal and make the flow field appear smooth. However, this will also lead to a potential bias in velocity estimates which is difficult to control. As the aim of this work is to quantify low blood velocities near the wall which would be significantly affected by residual clutter, filters were designed to strongly suppress the clutter signal, combined with tapering to reduce adverse filtering effects.

Limitations

Combining tissue signal from recorded data with flow signal from simulations was used for estimating the bias and variance of the velocity estimators. One limitation of this approach is that the ratio between clutter and noise signal in the synthetic data can not exceed that of the original data. Another limitation is that some of the clutter signal might have been removed by the low pass filter. Also, a more thorough validation could be performed including more complex flow scenarios. Nevertheless, this approach allowed assessment of the performance of the velocity estimators on a data set containing both realistic clutter signal and flow signal with known velocity profile.

The results in Fig. 13 illustrate a clear difference in behavior between upper and lower artery walls. Inspection of the right panels indicates that there is residual blood signal below the artery after filtering. This may be caused either by reverberations, or by the use of plane waves, which is associated with strong sidelobes and axial lobes in the point spread function. As a consequence, the blood signal in the vicinity of the lower wall will be affected by signal from more central blood flow with higher velocities. If the SNR is sufficiently high, no tapering or only weak tapering would be applied in this region. In the case shown in Fig. 13 this results in estimates showing high blood velocities also below the artery. This challenge cannot be addressed by tapered vector Doppler as formulated in this work, but motivates further work on suppressing reverberations and improving the point spread function.

All results indicate that the use of tapering may significantly improve the accuracy of low flow vector velocity estimation. The underlying assumption is that blood signal power from a region should be approximately equal for all receive directions, unless parts of the blood signal are in the stopband. This assumption might not always be valid, e.g if strong reflections from plaques lead to a reduction in signal power for some receive directions.

Potential applications

The results in Figure 12 indicate that the use of tapering has potential to improve estimation of wall shear rate. Accurate estimation of wall shear rate *in vivo* will also depend on robust extraction of the wall position for all frames, and a choice of suitable measurement parameters yielding consistent wall shear rate estimates. The contribution of tapering in this context is to reduce both bias and variance of low velocity estimates near the wall and make them less sensitive to filtering parameters.

Although tapered Vector Doppler was validated using a specific acquisition setup in this work, the technique is general

and could easily be used in regular cross-beam vector Doppler or other vector Doppler setups. In this work, tapering was applied to a processing chain originally designed for aliasing correction, yielding a vector velocity estimation scheme with improved robustness for both high and low blood velocities. As the inclusion of the tapering step only implies weighting of autocorrelation estimates, it is a computationally cheap approach to improve the accuracy of low flow velocity estimation without the use of regularization or prior assumptions on the flow field.

VI. CONCLUSION

A new method for vector velocity estimation, termed Tapered Vector Doppler, has been presented, to account for the removal of blood signal due to clutter filtering. The performance of the method was assessed using both simple and more realistic simulations, and *in vivo* feasibility was shown. Several tapering approaches were investigated, with soft tapering using R(1) signal power yielding the lowest variance for low velocity blood flow. All results indicate that Tapered Vector Doppler enables vector velocity estimates less affected by clutter and clutter filtering than what can be obtained by adaptive filter design only. This facilitates quantitative analysis of low velocity blood flow without the use of regularization techniques.

REFERENCES

- [1] M. Tanter, J. Bercoff, L. Sandrin, and M. Fink, "Ultrafast compound imaging for 2-D motion vector estimation: Application to transient elastography," *IEEE transactions on ultrasonics, ferroelectrics, and frequency control*, vol. 49, no. 10, pp. 1363–1374, 2002.
- [2] S. Salles, A. J. Y. Chee, D. Garcia, A. C. H. Yu, D. Vray, and H. Liebgott, "2-D arterial wall motion imaging using ultrafast ultrasound and transverse oscillations," *IEEE Transactions on Ultrasonics, Ferroelectrics, and Frequency Control*, vol. 62, no. 6, pp. 1047–1058, June 2015.
- [3] L. Løvstakken, S. A. Nyrnes, B. O. Haugen, and H. Torp, "Angle-independent quantification of complex flow patterns in congenital heart disease," in *2011 IEEE International Ultrasonics Symposium*, Oct 2011, pp. 1246–1249.
- [4] S. Fadnes, M. S. Wigen, S. A. Nyrnes, and L. Løvstakken, "In vivo intracardiac vector flow imaging using phased array transducers for pediatric cardiology," *IEEE transactions on ultrasonics, ferroelectrics, and frequency control*, vol. 64, no. 9, pp. 1318–1326, 2017.
- [5] K. L. Hansen, M. M. Pedersen, H. Møller-Sørensen, J. Kjaergaard, J. C. Nilsson, J. T. Lund, J. A. Jensen, and M. B. Nielsen, "Intraoperative cardiac ultrasound examination using vector flow imaging," *Ultrasonic imaging*, vol. 35, no. 4, pp. 318–332, 2013.
- [6] M. S. Wigen, S. Fadnes, A. Rodriguez-Molares, T. Bjåstad, M. Eriksen, K. H. Stensæth, A. Støylen, and L. Løvstakken, "4-D Intracardiac Ultrasound Vector Flow Imaging—Feasibility and Comparison to Phase-Contrast MRI," *IEEE transactions on medical imaging*, vol. 37, no. 12, pp. 2619–2629, 2018.
- [7] K. L. Hansen, J. Udesen, F. Gran, J. A. Jensen, and M. B. Nielsen, "In-vivo examples of flow patterns with the fast vector velocity ultrasound method," *Ultraschall in der Medizin-Europan Journal of Ultrasound*, vol. 30, no. 05, pp. 471–477, 2009.
- [8] I. K. Ekroll, T. Dahl, H. Torp, and L. Løvstakken, "Combined vector velocity and spectral Doppler imaging for improved imaging of complex blood flow in the carotid arteries," *Ultrasound in medicine & biology*, vol. 40, no. 7, pp. 1629–1640, 2014.
- [9] B. Y. Yiu, S. S. Lai, and C. Alfred, "Vector projectile imaging: Time-resolved dynamic visualization of complex flow patterns," *Ultrasound in medicine & biology*, vol. 40, no. 9, pp. 2295–2309, 2014.

- [10] K. L. Hansen, H. Møller-Sørensen, J. Kjaergaard, M. B. Jensen, J. T. Lund, M. M. Pedersen, T. Lange, J. A. Jensen, and M. B. Nielsen, "Analysis of Systolic Backflow and Secondary Helical Blood Flow in the Ascending Aorta Using Vector Flow Imaging," *Ultrasound in Medicine & Biology*, vol. 42, no. 4, pp. 899 – 908, 2016. [Online]. Available: <http://www.sciencedirect.com/science/article/pii/S0301562915007292>
- [11] K. Itatani, T. Okada, T. Uejima, T. Tanaka, M. Ono, K. Miyaji, and K. Takenaka, "Intraventricular Flow Velocity Vector Visualization Based on the Continuity Equation and Measurements of Vorticity and Wall Shear Stress," *Japanese Journal of Applied Physics*, vol. 52, no. 7S, p. 07HF16, jul 2013. [Online]. Available: <https://doi.org/10.7567>
- [12] J. Faurie, M. Baudet, K. C. Assi, D. Auger, G. Gilbert, F. Tournoux, and D. Garcia, "Intracardiac Vortex Dynamics by High-Frame-Rate Doppler Vortography In Vivo Comparison With Vector Flow Mapping and 4-D Flow MRI," *IEEE Transactions on Ultrasonics, Ferroelectrics, and Frequency Control*, vol. 64, no. 2, pp. 424–432, Feb 2017.
- [13] M. M. Pedersen, M. J. Pihl, P. Haugaard, K. L. Hansen, T. Lange, L. Lnn, M. B. Nielsen, and J. A. Jensen, "Novel Flow Quantification of the Carotid Bulb and the Common Carotid Artery with Vector Flow Ultrasound," *Ultrasound in Medicine & Biology*, vol. 40, no. 11, pp. 2700 – 2706, 2014. [Online]. Available: <http://www.sciencedirect.com/science/article/pii/S0301562914003895>
- [14] J. Avdal, L. Løvstakken, H. Torp, and I. K. Ekroll, "Combined 2-D Vector Velocity Imaging and Tracking Doppler for Improved Vascular Blood Velocity Quantification," *IEEE Transactions on Ultrasonics, Ferroelectrics, and Frequency Control*, vol. 64, no. 12, pp. 1795–1804, Dec 2017.
- [15] P. Tortoli, M. Lenge, D. Righi, G. Ciuti, H. Liebgott, and S. Ricci, "Comparison of Carotid Artery Blood Velocity Measurements by Vector and Standard Doppler Approaches," *Ultrasound in Medicine & Biology*, vol. 41, no. 5, pp. 1354 – 1362, 2015. [Online]. Available: <http://www.sciencedirect.com/science/article/pii/S0301562915000393>
- [16] M. Correia, J. Provost, M. Tanter, and M. Pernot, "4D ultrafast ultrasound flow imaging: in vivo quantification of arterial volumetric flow rate in a single heartbeat," *Physics in Medicine & Biology*, vol. 61, no. 23, p. L48, 2016.
- [17] P. Tortoli, T. Morganti, G. Bambi, C. Palombo, and K. V. Ramnarine, "Noninvasive simultaneous assessment of wall shear rate and wall distension in carotid arteries," *Ultrasound in medicine & biology*, vol. 32, no. 11, pp. 1661–1670, 2006.
- [18] R. S. Reneman and A. P. Hoeks, "Wall shear stress as measured in vivo: consequences for the design of the arterial system," *Medical & biological engineering & computing*, vol. 46, no. 5, pp. 499–507, 2008.
- [19] D. Garcia, J. C. del Iamo, D. Tann, R. Yotti, C. Cortina, . Bertrand, J. C. Antoranz, E. Prez-David, R. Rieu, F. Fernandez-Aviles, and J. Bermejo, "Two-Dimensional Intraventricular Flow Mapping by Digital Processing Conventional Color-Doppler Echocardiography Images," *IEEE Transactions on Medical Imaging*, vol. 29, no. 10, pp. 1701–1713, Oct 2010.
- [20] T. Grønli, M. Wiggen, P. Segers, and L. Løvstakken, "A Fast 4D B-Spline Framework for Model-Based Reconstruction and Regularization in Vector Flow Imaging," in *2018 IEEE International Ultrasonics Symposium (IUS)*, Oct 2018, pp. 1–9.
- [21] S. Ricci, A. Swillens, A. Ramalli, P. Segers, and P. Tortoli, "Wall shear rate measurement: Validation of a new method through multiphysics simulations," *IEEE transactions on ultrasonics, ferroelectrics, and frequency control*, vol. 64, no. 1, pp. 66–77, 2016.
- [22] P. Song, A. Manduca, J. D. Trzasko, and S. Chen, "Ultrasound small vessel imaging with block-wise adaptive local clutter filtering," *IEEE transactions on medical imaging*, vol. 36, no. 1, pp. 251–262, 2016.
- [23] J. Baranger, B. Arnal, F. Perren, O. Baud, M. Tanter, and C. Demené, "Adaptive spatiotemporal SVD clutter filtering for ultrafast Doppler imaging using similarity of spatial singular vectors," *IEEE transactions on medical imaging*, vol. 37, no. 7, pp. 1574–1586, 2018.
- [24] H. Torp, "Clutter rejection filters in color flow imaging: A theoretical approach," *IEEE transactions on ultrasonics, ferroelectrics, and frequency control*, vol. 44, no. 2, pp. 417–424, 1997.
- [25] K. C. Koskinas, Y. S. Chatzizisis, A. B. Baker, E. R. Edelman, P. H. Stone, and C. L. Feldman, "The role of low endothelial shear stress in the conversion of atherosclerotic lesions from stable to unstable plaque," *Current opinion in cardiology*, vol. 24, no. 6, pp. 580–590, 2009.
- [26] C. Slager, J. Wentzel, F. Gijssen, J. Schuurbiers, A. Van der Wal, A. Van der Steen, and P. Serruys, "The role of shear stress in the generation of rupture-prone vulnerable plaques," *Nature clinical practice Cardiovascular medicine*, vol. 2, no. 8, pp. 401–407, 2005.
- [27] C. Kasai, K. Namekawa, A. Koyano, and R. Omoto, "Real-time two-dimensional blood flow imaging using an autocorrelation technique," *IEEE Transactions on sonics and ultrasonics*, vol. 32, no. 3, pp. 458–464, 1985.
- [28] I. K. Ekroll, J. Avdal, A. Swillens, H. Torp, and L. Løvstakken, "An extended least squares method for aliasing-resistant vector velocity estimation," *IEEE transactions on ultrasonics, ferroelectrics, and frequency control*, vol. 63, no. 11, pp. 1745–1757, 2016.
- [29] J. A. Jensen, "Field: A program for simulating ultrasound systems," in *10th nordicbaltic conference on biomedical imaging, vol. 4, supplement 1, part 1: 351–353*. Citeseer, 1996.
- [30] J. A. Jensen and N. B. Svendsen, "Calculation of pressure fields from arbitrarily shaped, apodized, and excited ultrasound transducers," *IEEE transactions on ultrasonics, ferroelectrics, and frequency control*, vol. 39, no. 2, pp. 262–267, 1992.